Improvement of ZnO/Si Heterojunctions With a Coaxial Circular Transmission Line Model Applicable to Both Ohmic and Schottky

Norihiro Miyazawa, Naoto Usami, *Member, IEEE*, Haibin Wang, Takaya Kubo, Hiroshi Segawa, Takahito Takeda, Masaki Kobayashi, Yoshio Mita, *Senior Member, IEEE*, and Akio Higo, *Member, IEEE*

***Abstract*—Investigating heterointerfaces with test structures is crucial for fabricating electronic and photonic devices. Recently, we proposed and developed a PbS colloidal quantum dot/ZnO/Si hybrid infrared detector for infrared-sensitive optoelectronic devices on silicon-based large-scale integrated circuits. The conventional circular transfer length method (CTLM) is commonly used for evaluating Ohmic contact. To apply the CTLM to a heterointerface junction, we propose a coaxial CTLM (CCTLM) that includes a circular electrode in the middle and doughnut-shaped outer contact electrodes. The proposed test structure can be identified and quantitatively analyzed for the junction type (Ohmic or Schottky) by changing the electrode area. By using the CCTLM test structure for n-type ZnO/n-type Si heterojunctions and X-ray photoemission spectroscopy measurements, we identified the heterojunction as the Schottky type via the CCTLM and estimated the band diagram of the heterojunction.**

***Index Terms*—Heterojunctions, Schottky diodes, diodes, TLM method.**

I. Introduction

SILICON devices can be integrated with III-V compound semiconductor materials to achieve specific absorption characteristics, allowing the creation of a variety of remarkable sensor devices. For example, very large-scale integrated circuit (VLSI)-based image sensors for infrared (IR) wavelengths have various applications such as night vision, light detection and ranging(LiDAR) and even healthcare [1]–[6]. The conventional method of integration is direct epitaxial growth of the III-V compound semiconductor on Si; however, lattice mismatch hinders this process. The other approach is to bond the III-V compound semiconductor material and Si with a polymer layer, benzocyclobutene (BCB) glue, which is widely used for active and passive heterointegration such as laser diodes and Si photonic integrated applications [7]. However, obtaining large III-V compound wafers is still challenging.

As a revolutionary alternative, we investigate a PbS colloidal quantum dot (CQD) coating on silicon for IR absorption. PbS CQDs can be integrated on Si via inkjet-printing [8], spraycoating [9], spincoating [10] and dip coating [11]. These processes are LSI-compatible, scalable, low cost, and can be implemented at low temperatures. The absorption bandgap can be tuned based on molecular design (such as size). The integration of several optoelectronic devices has been studied, such as laser diodes [12], solar cells [9]–[11], [13], [14], and complementary metal oxide semiconductors [15], wherein graphene is used as the carrier transportation and collection layer.

We fabricated a PbS CQDs/Si heterojunction for an IR-sensitive photodiode; however, the quantum efficiency exhibited by this junction was quite low [16], [17]. To improve the performance, a thin ZnO layer as a carrier collection layer was inserted between PbS/Si interface [13], [18], [19]. As a result, the carrier collection at the wavelength of 1.33 μm was higher than that at a PbS CQDs/Si heterojunction; however, the efficiency was still considerably lower than that obtained in previous studies [19] as well as that of the PbS/ZnO/F-doped tin oxide (FTO) device [20].

To investigate the cause of low current, we developed a test structure [21]. The circular transfer length method (CTLM) is a well-known test method for investigating materials by measuring the frontside electrodes (Fig. 1). However, the conventional CTLM presumes the Ohmic interface. To improve the CTLM such that it can be used to analyze either Ohmic or Schottky type interfaces, doughnut-shaped outer electrodes were employed. Current is regulated by the inverse of the surface area of the outer electrode, permitting analysis of the characteristics of the one-sided heterojunction. In this study, we first investigated the Al electrode and ZnO interface using conventional CTLM and verified its Ohmic characteristics. We then investigated the (Al-)ZnO/Si heterojunction using the proposed test structures and found that the interface exhibited

Manuscript received December 20, 2020; revised April 16, 2021; accepted May 19, 2021. Date of publication May 24, 2021; date of current version August 4, 2021. This work was supported in part by Japan Society for the Promotion of Science (JSPS) KAKENHI under Grant 18J10240 and Grant 16H04345; in part by French National Research Agency under Grant ANR-16-CE33-0022; in part by Core Research for Evolutional Science and Technology, Japan Science and Technology Agency (JST) under Grant JPMJCR20T2; in part by ISAS/JAXA Strategic Research Grant; in part by JST-CREST under Grant JPMJCR1815; and in part by the Spintronics Research Network of Japan (Spin-RNJ). *(Corresponding authors: Norihiro Miyazawa and Akio Higo.)*

Norihiro Miyazawa, Takahito Takeda, Masaki Kobayashi, and Yoshio Mita are with the Department of Electrical Engineering and Information Systems, The University of Tokyo, Tokyo 113-8656, Japan (e-mail: miyazawa@if.t.u-tokyo.ac.jp; mems@if.t.u-tokyo.ac.jp).

Naoto Usami was with the Department of Aeronautics and Astronautics, The University of Tokyo, Tokyo 113-8656, Japan. He is now with the Institute of Space and Astronautical Science (ISAS), Japan Aerospace Exploration Agency (JAXA), Sagamihara, Japan.

Haibin Wang, Takaya Kubo, and Hiroshi Segawa are with the Research Center for Advanced Science and Technology, The University of Tokyo, Tokyo 153-8902, Japan.

Akio Higo is with the Systems Design Lab, The University of Tokyo, Tokyo 113-0032, Japan.

Color versions of one or more figures in this article are available at https://doi.org/10.1109/TSM.2021.3083069.

Digital Object Identifier 10.1109/TSM.2021.3083069

This work is licensed under a Creative Commons Attribution-NonCommercial-NoDerivatives 4.0 License.
For more information, see https://creativecommons.org/licenses/by-nc-nd/4.0/

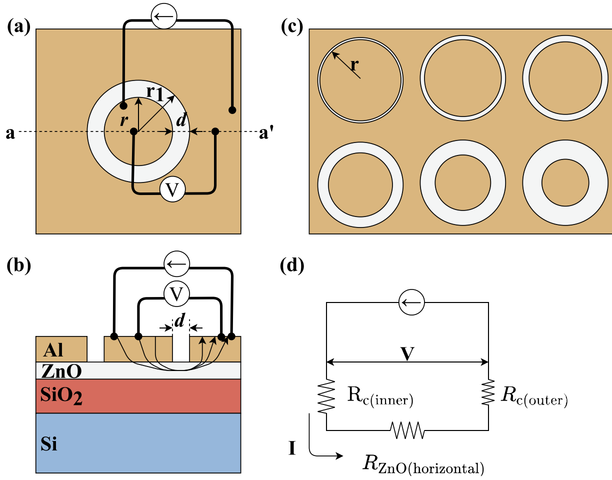

Fig. 1. Conventional CTLM patterns for Al/ZnO. The radius(r_1) of the central circle is fixed. d is changed and according to d, r changes. (a) Top view. (b) Cross-sectional view(a-a'). (c) All used patterns with variable gap spacing(d) of 5, 10, 15, 25, 35 and 45μm. (d) Equivalent circuit. The resistance of the outer contact area ($R_{c(outer)}$) is small because of its large size ($R_{c(inner)} \gg R_{c(outer)}$).

behaviors similar to that of the Schottky type; however, we expected an Ohmic interface because the polarity of ZnO and Si were both n-type. To confirm the Schottky behavior, X-ray photoemission spectroscopy (XPS) measurements were obtained.

We measured two types of test structures to investigate the Al/ZnO and ZnO/Si interfaces of the heterojunction device. We prepared two material configurations: (Device 1) Al/ZnO/SiO2/Si substrate and (Device 2) Al/ZnO/Si substrate. Device 1 investigates the Al/ZnO interface to extract its influence, and Device 2 the ZnO/Si interface.

II. Design of CCTLM

A. Conventional CTLM

A transmission line model (TLM) is traditionally used to extract the specific contact and sheet resistances of semiconductor materials [22]. The straight TLM pattern applied to the bulk material causes measurement errors due to the fringing effect. To avoid this effect, circular TLM (CTLM) was proposed and is now widely used [23], [24]. In this structure, the current flows isotropically between the inner and outer electrodes [25]. Figure 1 shows the conventional CTLM patterns; further, the expected current flow is shown in Fig. 1 (b). The total resistance, including the sheet resistance ($R_{s_{ZnO}}$) of ZnO and specific contact resistances ($R_{c_{Al/ZnO}}$), is estimated using equations (2) and (3), where R_{total} is the total resistance in Al/ZnO, L_T is the transfer length—through which the current flows in the semiconductor material, satisfying equation (3)—r_1 is a constant outer radius of the rings, and d is the gap spacing between electrodes in Fig. 1 (d).

$$R_{total} = R_{ZnO(horizontal)} + R_{c_{Al/ZnO(inner)}} + R_{c_{Al/ZnO(outer)}} \quad (1)$$

$$= \frac{R_{s_{ZnO}}}{2\pi}\left[\ln\left(\frac{r_1}{r_1 - d}\right) + L_T\left(\frac{1}{r_1} + \frac{1}{r_1 - d}\right)\right] \quad (2)$$

$$L_T \equiv \sqrt{\frac{R_{c_{Al/ZnO}}}{R_{s_{ZnO}}}} \quad (3)$$

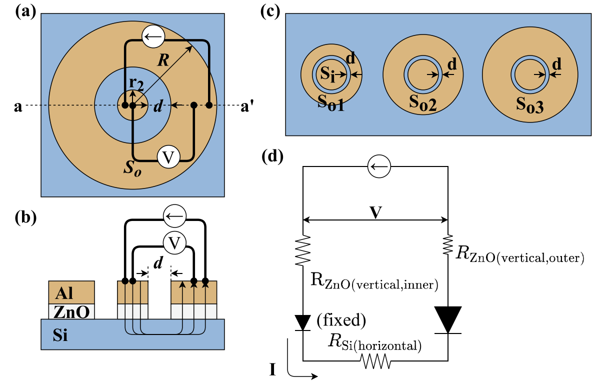

Fig. 2. Coaxial CTLM patterns for ZnO/Si. The radius(r_2) of the central circle is fixed. S(outer contact are) is changed. (a) Top view. (b) Cross-sectional view(a-a'). (c) All patterns used. (d) Equivalent circuit.

$$R_{c_{Al/ZnO}} \equiv R_{c_{Al/ZnO(inner)}} = R_{c_{Al/ZnO(outer)}}. \quad (4)$$

B. Proposed Coaxial CTLM

CTLM can also be used to identify whether the interface is Schottky or Ohmic type. A previous study determined the property of metal-semiconductor contacts with non-linear current–voltage (I–V) characteristics, using CTLM [26]. The I–V characteristics of the Schottky barrier diode are expressed using equation (5). However, in this previous study, the junction area (S) varied with the gap spacing. This caused variations in saturation current (I_s) in both side diodes, as shown in equation (6). The notations in the equation are as follows: n: ideality factor, A^{**}: Richardson constant, T: temperature, q: elementary charge, ϕ_B: barrier height, and k: Boltzmann constant.

$$I = I_{sat}(S)\left(e^{\frac{qV}{nkT}} - 1\right) \quad (5)$$

$$I_{sat}(S) = SA^{**}T^2 \exp\left(-\frac{q\phi_B}{kT}\right) \quad (6)$$

$$\left(A^{**} = \frac{4\pi m^* k^2 q}{h^3}\right) \quad (7)$$

To evaluate the interface of interest (ZnO/Si), as shown in Fig. 2, we propose a coaxial CTLM (CCTLM) structure and fabricate a single-side conventional microelectromechanical system (MEMS). While a through-the-wafer diode can be investigated via vertical measurements [27], this device requires an extra process to establish back-side contact. Therefore, the CCTLM makes this process easier by controlling the pattern design. This CCTLM test structure is highly compatible with CTLM and can be used irrespective of the interface (Schottky or ohmic).

The model of the interface is considered as shown in Fig. 2(d). Because it has diode components in both directions, they are added together.

C. Fabrication

We used the CTLM to determine the characteristics of the diodes or resistance. Each ring pattern in the CTLM had a constant outer radius of 200 μm and variable gap spacings of 5, 10, 15, 25, 35, and 45 μm. The CCTLM was used for evaluating the diode parameters. The area of the inner electrode was

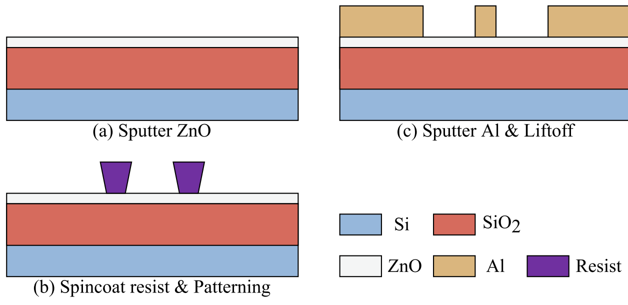

Fig. 3. Process flow chart in Al/ZnO to eliminate the influence of the electrode.

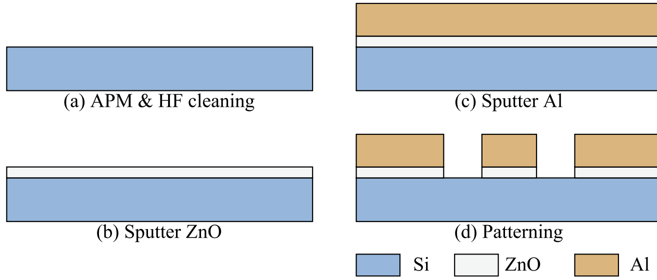

Fig. 4. Process flow chart of main target in ZnO/Si.

fixed at S_i. The area of the outer electrode was approximately two, four, and six times S_i in S_{o1}, S_{o2}, and S_{o3}, respectively.

The process for fabrication of device 1 is shown in Fig. 3. First, ZnO was sputtered onto 1 μm-thick SiO2 on 525 μm-thick n-type Si using a sputter tool (Shibaura Mechatronics Co. CFS-4ES), and the thickness of 64 nm was ensured using an ellipsometer (J.A. Woollam, M-2000DI-T). After the photoresist was spin-coated on the samples, the samples were patterned with six types of gaps using a laser direct lithography system (Heidelberg Instruments, DWL-66+). The Al (Al containing 1% Si) electrode was sputtered (ULVAC Inc., SIH-450), and patterns were formed via a lift-off process. Then, the Al thickness of 200 nm was ensured using a surface profiler (Bruker, DektakXT). Device 2 (Al/ZnO/Si) was fabricated as per the following procedure (Fig. 4): First, 525 μm-thick n-type Si with phosphorus-doped $3 \times 10^{14} \sim 4 \times 10^{15}$ was cleaned using an ammonium hydrogen peroxide mixture (APM), and the native oxide (SiO2) was removed using hydrofluoric acid (HF). Second, a 5 nm-thick ZnO layer was sputtered using the CFS-4ES to enable easy vertical flow of the current. Third, 200 nm-thick Al for the electrodes was sputtered using the SIH-450. Finally, Al and ZnO were patterned with three types of outer contact areas using the wet etchant, a mixture of phosphoric, nitric, and acetic acids (Kanto Chemical Co., Inc.). Overall, we fabricated three types for device 2. After that, device 1 with CTLM and device 2 with CCTLM were measured with the four-terminal measurement method as shown in Fig. 1 and Fig. 2.

III. Measurements and Analyses

A. Al/ZnO

The interface of Al/ZnO constitutes an Ohmic contact (see Fig. 5); here, the gap spacing and resistance showed a positive correlation, as shown in Fig. 6. Through equations (2) and (3), the specific contact resistance and sheet resistance of ZnO ($R_{s_{ZnO}}$) were calculated to be 3.4×10^{-1} Ωcm^2 and 1.3×10^8 Ω/sq, respectively. Subsequently, the sheet resistance gave rise to a ZnO resistivity of 8.3×10^2 Ωcm. The interface constitutes a low-resistance Ohmic contact, which is useful for eliminating the influence of the Al electrode from the final target structure (ZnO/Si).

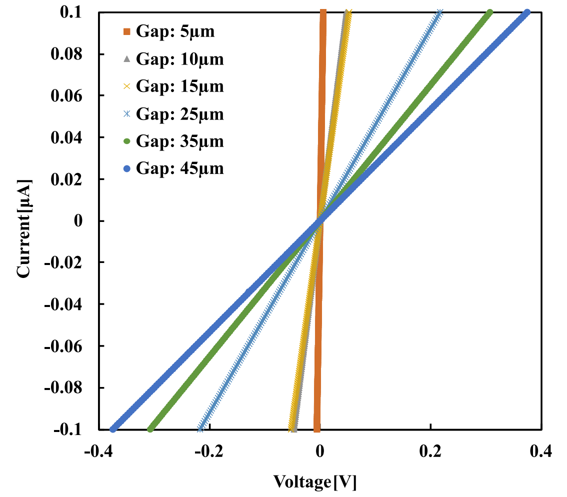

Fig. 5. The I-V characteristic in Al/ZnO. The thickness of ZnO is 64 nm.

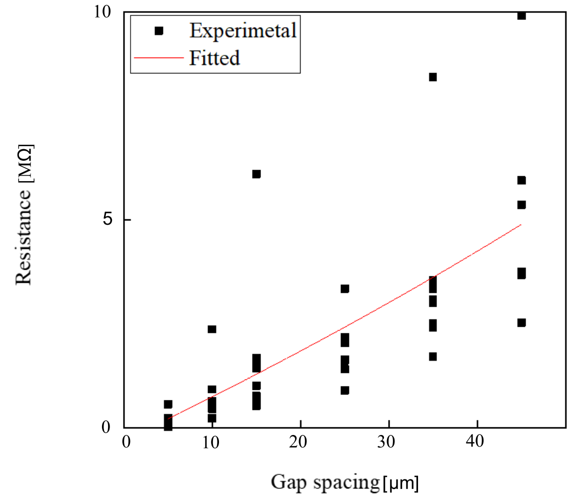

Fig. 6. Relationship between gap spacing and resistance as per the result of I-V measurements in Al/ZnO. The thickness of ZnO is 64 nm, and the discrepancy between the dimensions of the design and fabricated samples was considered.

B. ZnO/Si

The ZnO/Si interface behaved as a Schottky diode, as depicted in Fig. 7. The current at the same applied voltage increased with increasing outer contact area. In the forward bias region, the current was assumed to follow the saturation current, depending on the outer contact area. In contrast, in the reverse bias region, the current was constant and independent of the applied voltage, indicating that the interface behaved as a Schottky diode.

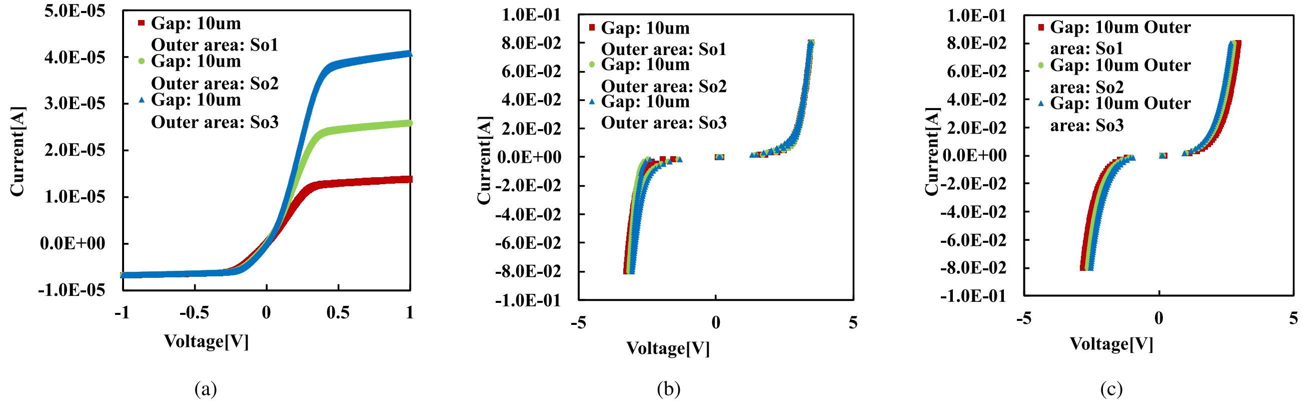

Fig. 7. The results of I-V measurement for ZnO/Si. The thickness of ZnO is 5 nm. The utilized Si substrates are (a) low-, (b) medium-, and (c) highly doped.

TABLE I
DOPING LEVEL

doping level	Resistivity (Ωcm)	Dopant
low-doped	1-10	P
medium-doped	0-0.02	P
high-doped	0.001-0.005	As

The slopes of the I-V curves are shown in Fig. 7 (a); when the outer contact area increases, each curve is saturated by outer areas. This indicates that the resistance and outer area have a negative correlation. The reason is below. As the outer electrode area increases, the current flowing vertically through the ZnO increases in the cross-sectional area. However, when the current reaches the Si, it must flow through the Si longer at the donut periphery than at the inner periphery to reach the inner island, which increases the resistance.

C. Doping Level Influence

We prepared samples of 5 nm ZnO under three different doping levels of Si. The Si used as described in the previous section had a resistivity of 1–10 Ω cm; however, the interface between the Si and the sputtered ZnO showed a rectifying effect. Therefore, we improved the band by changing the doping level. The corresponding amounts for each doping are shown in Table I.

Figure 7 (b) shows the result obtained on using the 525 μm thick n-Si with a resistivity of 0.0–0.02 Ω cm, and Fig. 7 (c) shows the results obtained on using n-Si with a higher doping level and a resistivity of 0.001–0.005 Ω cm. In this case, the current scaling increased when compared to the trend of the results for the sample, as depicted in Fig.7 (a), which was simultaneously sputtered with 5 nm thick ZnO. In contrast to Fig. 7 (a), Fig. 7 (b) and 7 (c) do not show the scale dependence of the saturation current. If Si is highly doped, the threshold voltage decreases when compared to that of the medium-doped one. Therefore, it is inferred that a good Ohmic contact was achieved at the interface with a high doping level.

D. X-Ray Photoemission Spectroscopy

CCTLM enabled the easier electrical evaluation of the Schottky contact interface. To support this result, we performed X-ray photoemission spectroscopy (XPS) measurements. XPS measurements were recorded using a Mg–Kα X-ray source ($h\nu = 1253.6$ eV), for which photoelectrons were collected using a Gammadata Scienta SES-100 hemispherical analyzer in the angle-integrated mode. The measurements were recorded at room temperature at a base pressure of approximately 1.0×10^{-7} Pa. The total resolution of the spectrometer was $\sim$ 200meV. The position of the Fermi level (E_F) was determined by measuring an Au foil in electrical contact with the sample.

To obtain the band diagram of the ZnO/Si heterostructure, the band bending near the interface was determined using XPS. Figure 8 shows the XPS spectra of the ZnO/Si films with ZnO thicknesses of 4 nm and 50 nm. As shown in Figs. 8(a) and 8(b), the peak positions of the Zn 2p spectra are nearly identical between the films, while the peak position of the Zn 3d spectrum of the 4 nm film is located 0.3 eV below that of the 50 nm film. Considering the kinetic energy dependence of the photoelectron mean free path [28], the probing depths of the Zn 2p and Zn 3d signals are 0.5—1 nm and 2—4nm, respectively. This suggests that the Zn 2p spectra are surface-sensitive and that the Zn 3d spectra are bulk-sensitive. Thus, the shift in the Zn 3d XPS spectra reflects the band bending of the ZnO layer near the interface between the ZnO layer and the Si substrate. The chemical potential shift near the interface was also observed in the valence band (VB) spectra, which are bulk-sensitive, as shown in Fig. 8(c).

The band bending of the Si substrate in the ZnO/Si film was also elucidated. Figure 9 shows the XPS spectra of the bare Si substrate and ZnO/Si films with ZnO thicknesses of 1.7 nm and 4 nm. Because of the sufficiently low thicknesses of the ZnO overlayers, the signals from the substrates could be measured. As shown in Fig. 9(a), there exist two kinds of Si signals in the Si 2p spectra, i.e., the signals from the Si-Si and Si-O bonding located at approximately 99 eV and 102—104 eV, respectively [29]. Compared to that of the Si 2p spectrum of the bare Si substrate, the Si-Si peak in the 4 nm film shifted to -0.15 eV. Notably, the Si-O peak shows a larger shift depending on the ZnO thickness compared to that of the Si-Si peak. This observation suggests that there exists an oxidized Si layer near the interface between the ZnO overlayer and the Si substrate, and the Si-O layer shows a

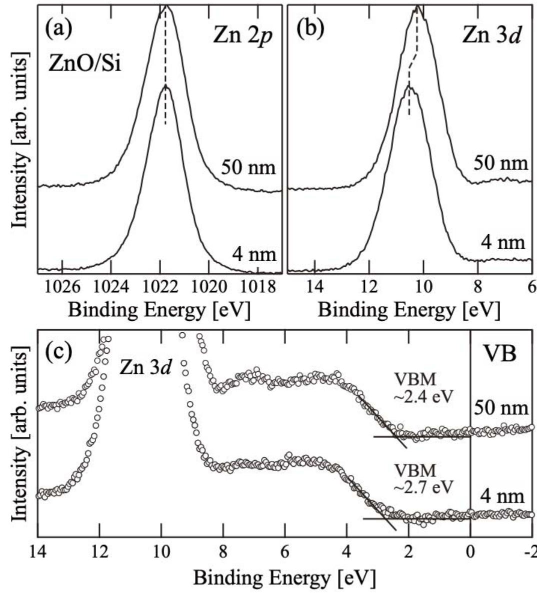

Fig. 8. Photoemission spectra of the ZnO layers in the ZnO/Si films. Here, the thicknesses of the ZnO layers are 4 nm and 50 nm. (a), (b) Zn 2p and Zn 3d XPS spectra, respectively. The vertical dashed lines denote the peak positions. (c) Valence band (VB) spectra. The VBM was estimated from the slopes of the VB spectra (see solid lines).

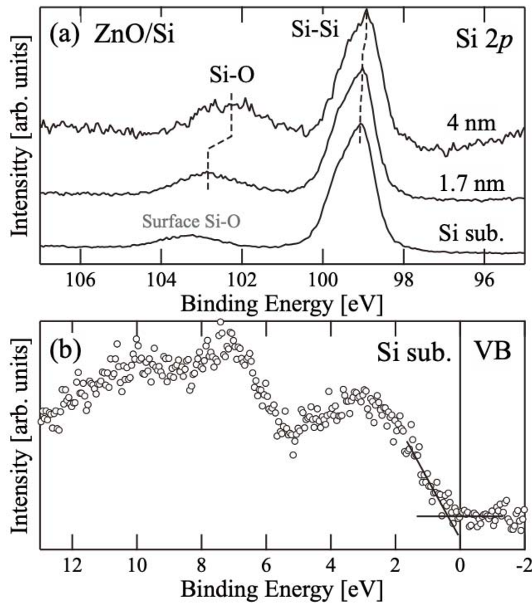

Fig. 9. Photoemission spectra of the Si substrates in the ZnO/Si films. (a) Si 2p XPS spectra. The spectra were obtained from the ZnO/Si films with ZnO thicknesses of 1.7 nm and 4 nm. The vertical dashed lines denote the peak positions. (b) VB spectra of the bare Si substrate. The solid lines denote the VBM.

larger chemical shift of ∼ –0.6 eV compared to the chemical potential shift or the band bending of the Si substrate. As shown in Fig. 9(b), the valence band maximum (VBM) of the Si substrate is located near E_F, indicating that the Si substrate is of p-type.

Based on the experiment, the band diagram of the ZnO/Si heterostructure was elucidated. Figure 10 shows the schematic band diagram of the ZnO/Si heterostructures. Note that the

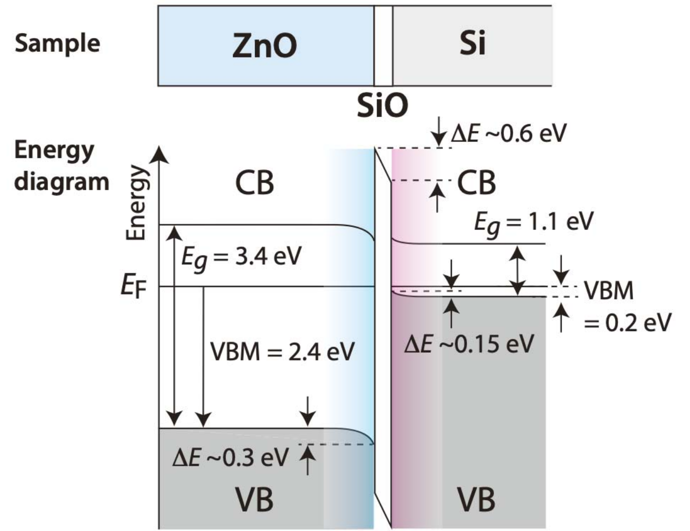

Fig. 10. Band diagram of ZnO/Si obtained from the XPS analysis. VB, CB, E_g, and E_F are the valence band, conduction band, band gap, and Fermi level, respectively.

band bending of the ZnO and Si bands near the interface are downward and upward, respectively, suggesting that carriers accumulate near the interface in ZnO/Si. These directions of the band bending in the ZnO/Si heterostructure are opposite to those in a conventional p-n junction with carrier depletion layers near the interface. The Si-O signals observed in the Si 2p spectra (see Fig. 9(a)) suggest that the ZnO layer and Si substrate are reduced (deoxidized) and oxidized near the interface, leading to the carrier accumulations. Thus, the appearance of the accumulation layers in ZnO/Si is probably due to the SiO interface layer. Because the I-V characteristics as determined via the CCTLM and XPS analysis indicated Schottky behavior at the ZnO/Si heterointerface, our proposed CCTLM is useful for heterojunction electrical analysis on a plane surface.

IV. Conclusion

A coaxial CTLM (CCTLM) was proposed in this study to determine the characteristic of the heterointerface with two diodes separated. A quantitative analysis of not only the Ohmic but also the Schottky behavior became possible by means of limiting the outer electrode area using a doughnut shape and then examining the current dependence on its surface area. Subsequently, the interface was identified to be not Ohmic but Schottky contact, and the characteristic of a single diode could be observed via the CTLM structure. The coaxial test structure required only single side lithography, which renders the fabrication process simpler.

We applied this method to the ZnO/Si interface, which is a part of a colloidal quantum dot IR-sensitive photodiode. To eliminate the influence of the Al electrode, Al/ZnO was measured using the conventional CTLM. The Ohmic characteristics were observed, and the ZnO/Si interface was investigated. The investigation indicated reverse-clamped diode characteristics; moreover, only the saturation current in one direction varied according to the outer doughnut electrode surface area. Finally, we realized the band diagram of the ZnO/Si heterojunction and

confirmed the Schottky behavior using the XPS measurements. Therefore, the usefulness of our simple test structure which needs only electrical analysis without expensive analysis such that XPS measurements, the CCTLM, was established.

ACKNOWLEDGMENT

The test structure design was supported by UTokyo d.lab, the University of Tokyo, in collaboration with Cadence Design Systems, Inc. The series processes were performed using the open facilities of UTokyo d.lab accessible through MEXT's Nanotechnology Platform Program.

REFERENCES

[1] T. Haruta *et al.*, "4.6 a 1/2.3 inch 20mpixel 3-layer stacked CMOS image sensor with DRAM," in *Proc. IEEE Int. Solid-State Circuits Conf. (ISSCC)*, 2017, pp. 76–77.

[2] H. Tsugawa *et al.*, "Pixel/DRAM/logic 3-layer stacked CMOS image sensor technology," in *Proc. IEEE Int. Electron Devices Meeting (IEDM)*, 2017, pp. 2–3.

[3] R. Thakur, "Scanning LIDAR in advanced driver assistance systems and beyond: Building a road map for next-generation LIDAR technology," *IEEE Consum. Electron. Mag.*, vol. 5, no. 3, pp. 48–54, Jul. 2016.

[4] S. Royo and M. Ballesta-Garcia, "An overview of lidar imaging systems for autonomous vehicles," *Appl. Sci.*, vol. 9, no. 19, p. 4093, 2019.

[5] S. Park *et al.*, "Ultraflexible near-infrared organic photodetectors for conformal photoplethysmogram sensors," *Adv. Mater.*, vol. 30, no. 34, 2018, Art. no. 1802359.

[6] H. Xu, J. Liu, J. Zhang, G. Zhou, N. Luo, and N. Zhao, "Flexible organic/inorganic hybrid near-infrared photoplethysmogram sensor for cardiovascular monitoring," *Adv. Mater.*, vol. 29, no. 31, 2017, Art. no. 1700975.

[7] B. Chen, W. Jiang, J. Yuan, A. L. Holmes, and B. M. Onat, "SWIR/MWIR InP-based pin photodiodes with InGaAs/GaaSSB type-II quantum wells," *IEEE J. Quant. Electron.*, vol. 47, no. 9, pp. 1244–1250, Sep. 2011.

[8] V. Wood *et al.*, "Inkjet-printed quantum dot–polymer composites for full-color AC-driven displays," *Adv. Mater.*, vol. 21, no. 21, pp. 2151–2155, 2009.

[9] I. J. Kramer *et al.*, "Efficient spray-coated colloidal quantum dot solar cells," *Adv. Mater.*, vol. 27, no. 1, pp. 116–121, 2015.

[10] S. A. McDonald *et al.*, "Solution-processed PbS quantum dot infrared photodetectors and photovoltaics," *Nat. Mater.*, vol. 4, no. 2, pp. 138–142, 2005.

[11] H. Wang, T. Kubo, J. Nakazaki, and H. Segawa, "Solution-processed short-wave infrared PbS colloidal quantum Dot/ZnO nanowire solar cells giving high open-circuit voltage," *ACS Energy Lett.*, vol. 2, no. 9, pp. 2110–2117, 2017.

[12] L. Li *et al.*, "Electrical pumping Fabry–Perot lasing of a III-V layer on a highly doped silicon micro rib," *Laser Phys. Lett.*, vol. 11, no. 11, 2014, Art. no. 115807.

[13] H. Wang, T. Kubo, J. Nakazaki, T. Kinoshita, and H. Segawa, "PbS-quantum-dot-based heterojunction solar cells utilizing ZnO nanowires for high external quantum efficiency in the near-infrared region," *J. Phys. Chem. Lett.*, vol. 4, no. 15, pp. 2455–2460, 2013.

[14] J. P. Clifford, G. Konstantatos, K. W. Johnston, S. Hoogland, L. Levina, and E. H. Sargent, "Fast, sensitive and spectrally tuneable colloidal-quantum-dot photodetectors," *Nat. Nanotechnol.*, vol. 4, no. 1, pp. 40–44, 2009.

[15] S. Goossens *et al.*, "Broadband image sensor array based on graphene–CMOS integration," *Nat. Photon.*, vol. 11, no. 6, pp. 366–371, 2017.

[16] A. Higo *et al.*, "Fabrication of PbS quantum dots and silicon device for near-infrared detection," in *Proc. Int. Conf. Opt. MEMS Nanophoton. (OMN)*, 2017, pp. 1–2.

[17] A. Higo *et al.*, "Fabrication of PbS QD/silicon hybrid infrared photodiode for LSI platform," *IEEJ Trans. Elect. Electron. Eng.*, vol. 138, no. 7, pp. 307–311, 2018.

[18] H. Wang *et al.*, "Enhanced carrier transport distance in colloidal PbS quantum-dot-based solar cells using ZnO nanowires," *J. Phys. Chem. C*, vol. 119, no. 49, pp. 27265–27274, 2015.

[19] S. Masala *et al.*, "The silicon: Colloidal quantum dot heterojunction," *Adv. Mater.*, vol. 27, no. 45, pp. 7445–7450, 2015.

[20] H. Wang, A. Higo, Y. Mita, T. Kubo, and H. Segawa, "PbS quantum Dot/ZnO nanowires hybrid test structures for infrared photodetector," in *Proc. IEEE 32nd Int. Conf. Microelectron. Test Struct. (ICMTS)*, 2019, pp. 8–11.

[21] N. Miyazawa *et al.*, "Coaxial circular test structure applicable to both ohmic and schottky characteristics for Zno/SI heterojunctions assessment," in *Proc. IEEE 33rd Int. Conf. Microelectron. Test Struct. (ICMTS)*, 2020, pp. 1–4.

[22] D. K. Schroder, *Semiconductor Material and Device Characterization*. New York, NY, USA: Wiley, 2015.

[23] G. Reeves, "Specific contact resistance using a circular transmission line model," *Solid-State Electron.*, vol. 23, no. 5, pp. 487–490, 1980.

[24] G. S. Marlow and M. B. Das, "The effects of contact size and non-zero metal resistance on the determination of specific contact resistance," *Solid-State Electron.*, vol. 25, no. 2, pp. 91–94, 1982.

[25] H. Yu *et al.*, "A simplified method for (circular) transmission line model simulation and ultralow contact resistivity extraction," *IEEE Electron Device Lett.*, vol. 35, no. 9, pp. 957–959, Sep. 2014.

[26] K. N. Patel, E. Stokes, J. Pagan, C. C. Burkhart, M. Hodge, and P. Batoni, "Circular transmission line model (CTLM) analysis for non-linear VI characteristics on Mg doped GaN," *ECS Trans.*, vol. 11, no. 5, pp. 203–208, 2007.

[27] S. N. Bystrova *et al.*, "Dealing with leakage current in TLM and CTLM structures with vertical junction isolation," in *Proc. Int. Conf. Microelectron. Test Structu. (ICMTS)*, 2017, pp. 1–6.

[28] S. Tanuma, C. Powell, and D. Penn, "Calculations of electron inelastic mean free paths. IX. Data for 41 elemental solids over the 50 ev to 30 kev range," *Surface Interface Anal.*, vol. 43, no. 3, pp. 689–713, 2011.

[29] A. Ohta, H. Murakami, M. Ikeda, K. Makihara, E. Ikenaga, and S. Miyazaki, "Potential changes and chemical bonding features for SI-MOS structure as evaluated from haxpes analysis," *Microelectron. Eng.*, vol. 178, pp. 80–84, Jun. 2017.